Novel Oscillation Suppression Methods for VSC-HVDC Island Sending Systems with Large Photovoltaic Power Integration

Yizhen Wang
State key laboratory of Smart Power Distribution Equipment and System
Tianjin University
Tianjin, China
yizhen.wang@tju.edu.cn

Xiang Xu
State key laboratory of Smart Power Distribution Equipment and System
Tianjin University
Tianjin, China
xiang_xu@tju.edu.cn

Yirun Ji
Electric Power Research Institute of State Grid Jibei Electric Power Co., Ltd.
Beijing, China
jiyirun@126.com

Zhiqian Wang
State key laboratory of Smart Power Distribution Equipment and System
Tianjin University
Tianjin, China
zhiqian_wang@tju.edu.cn

Yixin Zhang
State key laboratory of Smart Power Distribution Equipment and System
Tianjin University
Tianjin, China
yixin_03@tju.edu.cn

Xinyan Xu
State key laboratory of Smart Power Distribution Equipment and System
Tianjin University
Tianjin, China
xxy20030803@tju.edu.cn

***Abstract*— Voltage source converter high voltage direct current (VSC-HVDC) is a promising way to integrate large photovoltaic (PV). However, PV inverters tend to interact with long AC lines and VSC, causing wide-frequency oscillation problems. To improve the stability level of the VSC-HVDC island sending system, a novel oscillation suppression method is proposed. Firstly, oscillation mechanisms are analyzed via Bode plots based on PV inverter and VSC-HVDC impedance models. Secondly, PV inverter impedance is decomposed with corresponding adaptive control loops configured for each component. Finally, theoretical analysis and RT-LAB simulations are carried to verify the effectiveness and correctness of the proposed oscillation suppression method.**

Keywords—oscillation suppression, PV inverter, VSC-HVDC, adaptive control

I. INTRODUCTION

Amid the accelerated transition of the global energy structure toward cleanliness, new energy generation technologies represented by photovoltaic (PV) power have become as the core driving force for achieving the China's "dual-carbon" goals [1]. PV grid-connected power generation generally relies on long-distance transmission lines connected to high-voltage direct current (HVDC) systems for power delivery. However, a grid-following inverter (GFI) serving as the interface between PV systems and AC transmission lines tends to interact with voltage source converters (VSCs) under long AC transmission line scenarios, thereby triggering oscillations [2].

At present, numerous studies have analyzed the interactive effects among PV inverter, long AC transmission lines, and VSC. Ref. [3] indicates that the influence of the phase-locked loop (PLL) of GFI primarily manifests as a negative impedance effect in the q-axis current control loop. In [4], an impedance model is established for GFI in PV grid-connected systems to analyze the impact of long AC transmission lines, and a parameter design criteria is proposed under weak grid conditions. Through participation factor analysis, Ref. [5] finds that the interaction between the PLL of the PV inverter and the voltage loop control of the VSC induces subsynchronous oscillations (SSOs).

Currently, scholars have also proposed many oscillation suppression methods, which mainly include improved control strategies, optimized control parameters, installation of impedance adaptation devices at the point of common coupling (PCC), and introduction of additional control. Ref. [6] shows that an increase in PLL bandwidth intensifies the coupling between active power and reactive power control, and a derivative feedback compensation method is proposed to effectively suppress the instability caused by increased PLL bandwidth; however, the improvement achieved by this method is limited. In [7], a voltage feedforward control is proposed to offset the negative impedance effect caused by the PLL, nevertheless, a satisfactory oscillation suppression effect requires parameter adjustments with unclear physical meanings. In [8], a robust grid voltage feedforward scheme is proposed, which extracts the grid voltage from the grid-connected voltage and adopts a dual-sampling mode to improve the harmonic suppression capability and stability of GFI under weak grid conditions; however, the dual-sampling mode may be disturbed by switching noise under extreme duty cycles. In [9], a control method that combines the PLL with additional frequency control is proposed, which can effectively adapt to changes in grid impedance but requires adjusting proportional-integral-derivative (PID) parameters according to different operating conditions. Ref. [10] shows that introducing a first-order low-pass filter in the VSC voltage feedforward loop can suppress oscillations through impedance modeling and analysis on the VSC-HVDC connected systems; however, the improvement is limited when the AC transmission line is relatively long.

Based on the above research, this paper takes VSC-HVDC island sending systems with large PV power integration as the research object. Starting from the traditional dual closed-loop current control strategy, it establishes the PV inverter impedance model incorporating the PLL and the VSC impedance model, and designs an adaptive oscillation suppression strategy from the perspective of dynamically adapting to system characteristics and actively suppressing wide-frequency oscillations. Taking the Generalized Nyquist Stability Criterion (GNSC) as a constraint, this paper analyzes the PV inverter impedance and proposes corresponding adaptive control loops for each impedance link to suppress the interaction between PV inverter, AC lines, and VSC, thereby improving the stability

Supported by the National Natural Science Foundation of China (Grant No. 52377119 and U22B20109)

XXX-X-XXXX-XXXX-X/XX/$XX.00 ©20XX IEEE
979-8-3315-8138-1

of VSC-HVDC island sending systems with large PV power integration. The proposed adaptive control method can improve the system impedance according to the real-time operating state of the PV station transmitted via VSC-HVDC. Theoretical analysis using Nyquist plots shows that the proposed adaptive oscillation suppression method can ensure stable operation of PV over the full power range under long AC line lengths, with strong robustness. Finally, the effectiveness and correctness of the proposed strategy are verified by simulation in RT-LAB.

II. Modeling and Stability Analysis

A. Structure of VSC-HVDC Island Sending Systems with Large PV Power Integration

This paper focuses on the small-signal stability. The Fig. 1 is a schematic diagram of the VSC-HVDC island sending system with large PV power integration. The PV power station are stepped up to 110 kV through the generator-side transformer and the busbar transformer before being connected to the VSC-HVDC.

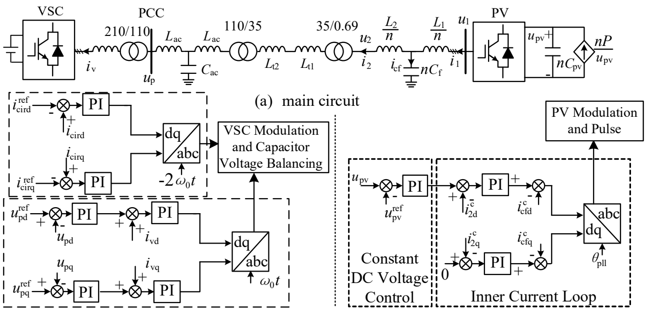

Fig. 1. Structure of PV-Connected VSC-HVDC Transmission System

In Fig. 1, the PV inverter adopts grid-following control and tracks the phase of the voltage u_2 on the low-voltage side of the collection bus generator terminal transformer through a PLL. The voltage outer loop adopts constant DC voltage control, and the current inner loop adopts the dual closed-loop current control strategy. LCL filter is used on the AC side, where L_1, L_2, and C_f are its inductors and capacitor. The reactances of the collection transformer and the generator terminal transformer are all referred to the 35kV bus side and are respectively incorporated into L_{t1} and L_{t2}. P is the output power of the PV power station, and C_{pv} is the DC capacitor of the VSC. The AC line is modeled using a T-type equivalent circuit, where L_{ac} and C_{ac} are the lumped inductance and capacitance parameters of the AC line, respectively.

All variables and models in this paper use per-unit values. A superscript "s" on a variable indicates that the variable is in the dq frame of the main system, while a superscript "c" indicates that it is in the dq coordinate system of the controller. For a transfer function G, if all variables contained within it are in the dq coordinate system of the main system, it is denoted as G^s; if all variables are in the dq coordinate system of the VSC control system, it is denoted as G^c. A subscript "0" on a variable in the lower right corner denotes the steady-state value.

B. Impedance Modeling of Equivalent PV Power Station

Ref. [11] establishes a linearized model at the steady-state point for the main circuit and control system of the equivalent PV power station. The impedance model of the equivalent PV power station can be derived as:

$$-G_I \Delta I_{2dq}^s + G_P \Delta P_{pv} = \left(G_{DC} + G_{AC\_s} + G_{AC\_pll}\right) \Delta U_{2dq}^s \quad (1)$$

Denote the admittance of the grid-connected PV inverter viewed from point u_2 to VSC when $\Delta P_{pv}=0$ as:

$$Y_O = G_I^{-1}\left(G_{DC} + G_{AC\_s} + G_{AC\_pll}\right) \quad (2)$$

the transfer functions are shown in the Appendix A1-A11.

C. Impedance Modeling of VSC

Ref. [12] establishes the analytical model for the main circuit and control system of VSC. Due to space limitations, the detailed modeling process will not be repeated here. The small-signal impedance model of VSC is Z_{VSC}.

D. Stability Analysis of VSC-HVDC Island Sending Systems with Large PV Power Integration

By integrating the above impedance models and considering AC line inductance and capacitance, the equivalent impedance viewed from the busbar to the VSC can be described as

$$Z_S = Z_{Lt12} + Y_{Cac} - Y_{Cac}\left(Z_{Lac} + Y_{Cac} + Z_{VSC}\right)^{-1} Y_{Cac} \quad (3)$$

The transfer function are given in the Appendix A2.

Combined with the PV inverter impedance equation, the expression of the grid-connected current is:

$$\Delta I_{2dq}^s = \left(Y_O Z_S + E\right)^{-1} G_I^{-1} G_P \Delta P \quad (4)$$

Assume that the PV grid-connected system can remain stable when the PV power station is directly connected to the infinite bus through a transformer, i.e., when $\Delta U_{2dq}^s = 0$, Equation (4) becomes:

$$\Delta I_{2dq}^s = \left(G_I\right)^{-1} G_P \Delta P_{pv} \quad (5)$$

Since the system can maintain small-signal stability, $\left(G_I\right)^{-1} G_P$ does not have unstable poles. Then, according to the GNSC, the stability of the system depends on $(Y_O Z_S+E)^{-1}$ in Equation(4) [13]. The Fig. 2 shows the Bode plots of the eigenvalues of $Y_O Z_S$ under different AC line lengths under the same operating condition, where the line lengths are 1 km and 24 km, respectively. With the AC line length increasing, the magnitude of $Y_O Z_S$ approximately shifts upward, resulting in a decrease in the cutoff frequency. It can be seen that the system with a longer line length has an instability problem.

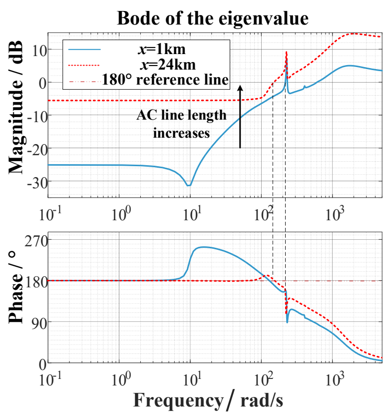

Fig. 2. The Bode plots of the eigenvalues of $Y_O Z_S$

III. Adaptive Oscillation Suppression Control Strategy and Its Stability Analysis

Based on the impedance model established above, this

979-8-3315-8138-1

paper introduces adaptive control into the PV control system to suppress the adverse effects of increased AC line length and enhance system damping. From the Bode plots of eigenvalues, the phase in the high-frequency band gradually approaches 0°, which is due to the same order of numerator and denominator in the eigenvalues of $Y_O Z_S$. Except for the time-delay transfer function, other transfer functions in the admittance Y_O of PV inverter can be approximately constructed. Therefore, a transfer function approximately identical to Y_O is constructed to reduce the mid-frequency magnitude of Y_O and shift the cutoff frequency to the high-frequency band.

A. Reducing the Magnitudes of G_{AC_s} and G_{AC_pll}

First, consider the coordinate transformation formula from ΔU_{2dq}^{c} to ΔU_{2dq}^{s}:

$$\Delta U_{2dq}^{s} = G_{pll}^{s} \Delta U_{2dq}^{c} \tag{6}$$

the G_{pll}^{s} is shown in the Appendix A8.

Then, In the small-signal range, $U_{2d}^{c} = U_{2d}^{s}$ and $U_{2q}^{c} = U_{2q}^{s} = 0$. Therefore, the element in the first row and second column of G_{pll}^{s} is 0, and $\Delta U_{2dq}^{s} = G_{pll}^{c} \Delta U_{2dq}^{c}$.

Consider the small-signal perturbation $G_{pll}^{c} U_{2dq}^{c}$:

$$\Delta\left(G_{pll}^{c} U_{2dq}^{c}\right) = \Delta G_{pll}^{c} \bullet \left(U_{2dq}^{c}\right)_0 + \left(G_{pll}^{c}\right)_0 \Delta U_{2dq}^{c} \tag{8}$$

Since $U_{2q}^{c} = 0$ at steady state, the first term in the above equation is 0. Thus, $\Delta\left(G_{pll}^{c} U_{2dq}^{c}\right) = \Delta U_{2dq}^{s}$.

Consider the small-signal perturbation of $G_{pll\_I2}^{c} G_{pll}^{c} U_{2dq}^{c}$:

$$\begin{aligned} &\Delta\left(G_{pll\_I2}^{c} G_{pll}^{c} U_{2dq}^{c}\right) \\ &= \Delta G_{pll\_I2}^{c} \bullet \left(G_{pll}^{c} U_{2dq}^{c}\right)_0 + \left(G_{pll\_I2}^{c}\right)_0 \bullet \Delta\left(G_{pll}^{c} U_{2dq}^{c}\right) \end{aligned} \tag{9}$$

Similarly, within the small-signal range, $U_{2q}^{c} = 0$, $I_{2d}^{c} = I_{2d}^{s}$, $I_{2q}^{c} = I_{2q}^{s}$, so $\Delta G_{pll\_I2}^{c} \bullet \left(G_{pll}^{c} U_{2dq}^{c}\right)_0 = 0$ .Therefore, $\Delta G_{pll\_I2}^{c} G_{pll}^{c} U_{2dq}^{c} = \Delta G_{pll\_I2}^{s} \Delta U_{2dq}^{s}$.

Similarly, within the small-signal range, $\Delta G_{pll\_Ic}^{c} G_{pll}^{c} U_{2dq}^{c} = G_{pll\_Ic}^{s} \Delta U_{2dq}^{s}$, $\Delta G_{pll\_U1}^{c} G_{pll}^{c} U_{2dq}^{c} = G_{pll\_U1}^{s} \Delta U_{2dq}^{s}$.

Consider introducing $G_1 = G_{PIi} G_{pll\_I2}^{c} G_{pll}^{c} U_{2dq}^{c}$, $G_2 = k_C G_{pll\_Ic}^{c} G_{pll}^{c} U_{2dq}^{c}$, and $G_3 = G_{pll\_U1}^{c} G_{pll}^{c} U_{2dq}^{c} / k_0$ into the control system, which can reduce G_{AC_pll}. Introducing $G_4 = (G_{u1u} / k_0 + k_C G_{icu}) G_{pll}^{c} U_{2dq}^{c}$ into the control system can reduce G_{AC_s}. However, G_{pll}^{c} contains a second-order integral, so an equivalent second-order high-pass filter F_0 can be added before $G_{pll}^{c} U_{2dq}^{c}$. The expression of F_0 is given in the Appendix A12.

Finally, the controller implementation issue needs to be considered. The transfer function must be proper. Therefore, the $G_{u1u} / k_0 + k_C Z_C$ in the G_4 needs to be replaced with the commonly used approximate derivative $s/(Ts+1)$ in engineering, where T is very small, generally taken as 0.01.

The construction of the controller is shown by the signal transmission of G_A, G_B, and G_C in Fig. 3, the expressions of which are given in the Appendix A13.

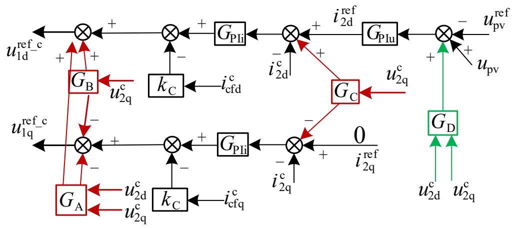

Fig. 3. The PV inverter control system incorporating adaptive control

B. Reducing the Impact of G_{DC}

We consider introducing $k_{dc} G_{PIu} G_{PIi} G_{dc}$ into the control system to reduce G_{DC}, where the expression of G_{dc} is:

$$G_{dc} = \frac{F_1 F_{dc}}{s} G_{PV} G_{pll\_new} U_{2dq}^{c} \tag{10}$$

where $G_{PV} = \left(U_{1dq}^{c}\right)^{T} Z_C + \left(I_{1dq}^{c}\right)^{T} G_{u1u}$; Considering the implementability of the controller, a first-order inertial loop F_1 is needed; Considering that the outer loop adopts constant DC voltage control with DC voltage tracking the command value and the existing integral loop, an equivalent second-order high-pass filter F_{dc} is needed. The above expressions are given in Appendix A12 and A15.

Consider the small perturbation ΔG_{dc}:

$$\begin{aligned} &\Delta G_{dc} \\ &= \frac{k_{dc} F_1 F_{dc}}{s} \left\{ \begin{aligned} &\left[\left(U_{1dq}^{c}\right)_0^{T} Z_C + \left(I_{1dq}^{c}\right)_0^{T} G_{u1u}\right] (G_{pll\_new})_0 \Delta U_{2dq}^{s} \\ &+ \Delta\left(U_{1dq}^{c}\right)^{T} \bullet \left(Z_C G_{pll\_new} \Delta U_{2dq}^{s}\right)_0 \\ &+ \Delta\left(I_{1dq}^{c}\right)^{T} \bullet \left(G_{u1u} G_{pll\_new} \Delta U_{2dq}^{s}\right)_0 \end{aligned} \right\} \end{aligned} \tag{11}$$

Due to the influence of G_{pll_new}, the steady-state values of $Z_C G_{pll\_new} \Delta U_{2dq}^{s}$ and $G_{u1u} G_{pll\_new} \Delta U_{2dq}^{s}$ are zero. Therefore, $\Delta G_{dc} = k_{dc} F_1 F_{dc} \left[\left(U_{1dq}^{c}\right)_0^{T} Z_C + \left(I_{1dq}^{c}\right)_0^{T} G_{u1u}\right] G_{pll\_new} \Delta U_{2dq}^{s} / s$.

Finally, the connection of the actual control loop that needs to be designed is shown as G_D in Fig. 3, and the expression of G_D is given in the Appendix A13.

C. Stability Analysis of the System After Introducing Adaptive Control

By performing impedance modeling analysis on the system after introducing adaptive control, the new PV inverter impedance can be obtained as:

$$Y_{O\_new} = G_I^{-1} G_{U\_new} \tag{12}$$

The expressions of G_{U_new} are given in the Appendix A14-A16. The selections of ω_0 and ω_{dc} for F_0 and F_{dc} in the filters should be greater than 5. And ω_0 needs to be smaller than the cutoff frequency ω_c without additional control, and ω_{dc} needs to be smaller than ω_0. T_1 can be taken as 0.01.

Fig. 4 shows the Nyquist plots of the eigenvalues of $Y_O Z_S$ (with dual closed-loop current control and voltage feedforward control [7]) and $Y_{O\_new} Z_S$ (with the proposed adaptive control strategy) under 24km AC line (only considering the curves of eigenvalues closer to the (-1, j0) point). Other parameters are the same. The parameters of dual closed-loop current control and adaptive control are shown in the Appendix Table.

As can be seen from the Fig. 4, under the condition of high PV output power, traditional control cannot ensure stable power output, while the improvement in system stability of voltage feedforward control is limited; by contrast, the adaptive control strategy proposed in this paper can ensure the PV system operates stably over the full power range and has a large stability margin.

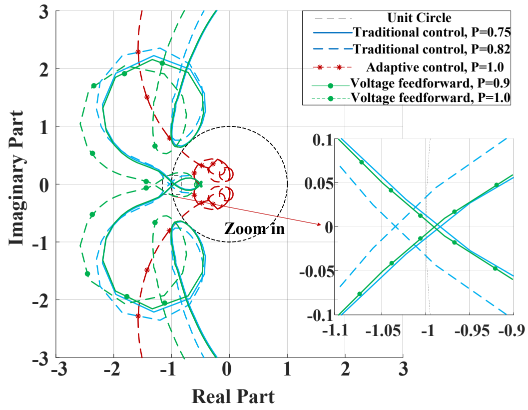

Fig. 4. The Nyquist comparison plots of the eigenvalues of $Y_O Z_S$

IV. Case Study

A. Small-Signal Model Verification

The equivalent model of the PV power station shown in Fig. 1 is built in RT-LAB, and the control system is implemented in DSP28335, as shown in Fig. 5, to verify the accuracy of the small-signal model of the PV power station connected to the VSC-HVDC transmission system established in Section I. The AC line is set to 1 km, and other system parameters and control parameters are detailed in supplementary Tables in the Appendix Table. At the initial moment, the PV power station outputs 0.8p.u. active power; at t=1.1 s, its output active power steps to 0.9p.u..

(a) (b) (c)

Fig. 5. (a) RT-LAB simulator (b) Interface between controller and RT-LAB (c) Control system of photovoltaic power station

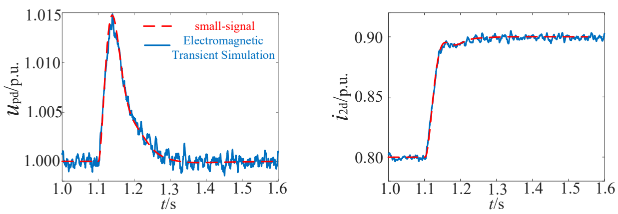

(a) d-axis voltage at the PCC (b) d-axis current of the VSC

Fig. 6. The verification of the small-signal model

Fig. 6(a) and (b) are the comparison diagrams of the d-axis voltage at the PCC point and the d-axis output current of the PV inverter between the electromagnetic transient model and the mathematical model, respectively. As can be seen from Fig. 6, the electromagnetic transient simulation results are consistent with the simulation results of the small-signal model established in Section I, which verifies the accuracy of the established small-signal model.

B. Verification of Traditional Dual Closed-Loop Current Control Strategy and Adaptive Control Strategy

Simulation settings for the traditional dual closed-loop current control: In the steady state, the power is set to 0.75p.u., and steps to 0.82p.u. at t=0.1s. Simulation settings for the adaptive control proposed in this paper: In the steady state, the power is set to 0.9p.u., and steps to 1p.u. at t=0.1s. The PV inverter DC voltages of both are shown in Fig. 7. As can be seen from the Fig. 7, the PV grid-connected system with adaptive control incorporated can operate stably under this operating condition, which is consistent with the results of impedance stability analysis.

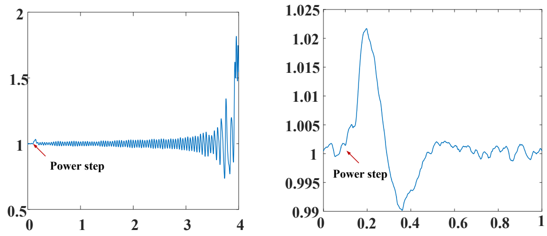

(a) DC voltage under traditional control (b) DC voltage under adaptive control

Fig. 7. Simulation of PV-Connected MMC-HVDC Transmission System

V. Conclusion And Future Works

To address the small-signal stability issue of VSC-HVDC island sending systems with large PV power integration, this paper proposes an adaptive control strategy. The conclusions are as follows:

1) This paper derives the dq impedance transfer function matrices of PV inverter and VSC. When the AC line length increases, the Nyquist curves of the eigenvalues of $Y_O Z_S$ have the instability risk of encircling the (-1, j0) point.

2) This paper proposes an adaptive control architecture. By introducing the adaptive control structure, it dynamically compensates the system impedance. The GNSC proves that the proposed control strategy still has a good stability margin.

3) This paper conducts RT-LAB simulation experiments, which verify that the proposed strategy effectively suppresses oscillations, improving system damping, and provides a stable control scheme with both theoretical depth and engineering feasibility for high-penetration PV grid connection.

In the future, the impact of different VSC control structures and parameters on the adaptive control strategy of PV inverter will be investigated.

Acknowledgment

This work is supported by the National Natural Science Foundation of China (Grant No. 52377119 and U22B20109).

References

[1] N. Flourentzou, V. G. Agelidis and G. D. Demetriades, "VSC-Based HVDC Power Transmission Systems: An Overview," IEEE Transactions on Power Electronics, vol. 24, no. 3, pp. 592-602, March 2009.

[2] C. Yin, X. Li, B. Yuan and J. Lai, "A review of the high frequency oscillation phenomena in VSC-HVDC power transmission system,"

2022 Annual Meeting of CSEE Study Committee of HVDC and Power Electronics (HVDC 2022), Guangzhou, China, 2022, pp. 183-191.

[3] X. Jiang, S. Yang, Z. Cai and N. Yao, "Stability Analysis and Improvement of Symmetric PLL-Based VSC in Weak Grids," 2024 IEEE International Conference on Electrical Energy Conversion Systems and Control（IEECSC), Shanghai, China, 2024, pp. 207-211.

[4] D. Zhu, S. Zhou, X. Zou and Y. Kang, "Improved Design of PLL Controller for LCL-Type Grid-Connected Converter in Weak Grid," in IEEE Transactions on Power Electronics, vol. 35, no. 5, pp. 4715-4727, May 2020.

[5] Y. Wang, C. Zhao, C. Guo and A. U. Rehman, "Dynamics and small signal stability analysis of PMSG-based wind farm with an MMC-HVDC system," in CSEE Journal of Power and Energy Systems, vol. 6, no. 1, pp. 226-235, March 2020.

[6] C. Guo, S. Yang, W. Liu, C. Zhao and J. Hu, "Small-Signal Stability Enhancement Approach for VSC-HVDC System Under Weak AC Grid Conditions Based on Single-Input Single-Output Transfer Function Model," in IEEE Transactions on Power Delivery, vol. 36, no. 3, pp. 1313-1323, June 2021.

[7] D. Zhu, S. Zhou, X. Zou, Y. Kang and K. Zou, "Small-Signal Disturbance Compensation Control for LCL-Type Grid-Connected Converter in Weak Grid," in IEEE Transactions on Industry Applications, vol. 56, no. 3, pp. 2852-2861, May-June 2020.

[8] X. Xia, L. Yang, S. Qiao, D. Kong, J. Chen and S. Chen, "Robust Control Method for LCL-Type Grid-Connected Inverters Based on Adaptive Correction of Grid Voltage Feedforward Considering Digital Control Delay," 2023 IEEE 7th Conference on Energy Internet and Energy System Integration (EI2), Hangzhou, China, 2023, pp. 2923-2928.

[9] M. Zhang and L. Sun, "PLL and Additional Frequency Control Constituting an Adaptive Synchronization Mechanism for VSCs," in IEEE Transactions on Power Systems, vol. 35, no. 6, pp. 4920-4923, Nov. 2020.

[10] L. Yang, Y. Zhu, S. Lin, K. Luan, W. Huang and Y. He, "Oscillation Suppressing Control Method Based on Impedance Optimization for Grid-Connected VSC-HVDC System," 2023 International Conference on Power System Technology (PowerCon), Jinan, China, 2023, pp. 1-7.

[11] S. Golestan, E. Ebrahimzadeh, B. Wen, J. M. Guerrero and J. C. Vasquez, "dq-Frame Impedance Modeling of Three-Phase Grid-Tied Voltage Source Converters Equipped With Advanced PLLs," in IEEE Transactions on Power Electronics, vol. 36, no. 3, pp. 3524-3539, March 2021.

[12] T. Xue, J. Lyu, H. Wang and X. Cai, "A Complete Impedance Model of a PMSG-Based Wind Energy Conversion System and Its Effect On the Stability Analysis of MMC-HVDC Connected Offshore Wind Farms," in IEEE Transactions on Energy Conversion, vol. 36, no. 4, pp. 3449-3461, Dec. 2021.

[13] L. Guan, J. Yao, R. Liu, P. Sun and S. Gou, "Small-Signal Stability Analysis and Enhanced Control Strategy for VSC System During Weak-Grid Asymmetric Faults," in IEEE Transactions on Sustainable Energy, vol. 12, no. 4, pp. 2074-2085, Oct. 2021.

APPENDIX

LCL filter, transformer inductor, and AC line impedance:

$$G_{\omega}=\begin{bmatrix} s & -\omega \\ \omega & s \end{bmatrix}, G_{\omega}^{*}=\begin{bmatrix} s^{*} & -\omega \\ \omega & s^{*} \end{bmatrix}, s^{*}=\frac{s}{0.01s+1} \tag{A1}$$

$$\begin{cases} Z_{\mathrm{L1}}=L_1 G_{\omega}, Z_{\mathrm{L2}}=L_2 G_{\omega}, Z_{\mathrm{C}}=C_{\mathrm{f}} G_{\omega} \\ Z_{\mathrm{Lt12}}=\left(L_{\mathrm{t1}}+L_{\mathrm{t2}}\right) G_{\omega}, Z_{\mathrm{Lac}}=L_{\mathrm{ac}} G_{\omega}, Z_{\mathrm{Cac}}=C_{\mathrm{ac}} G_{\omega} \\ Z_{\mathrm{L1}}^{*}=L_1 G_{\omega}^{*}, Z_{\mathrm{L2}}^{*}=L_2 G_{\omega}^{*}, Z_{\mathrm{C}}^{*}=C G_{\omega}^{*} \end{cases} \tag{A2}$$

$$\begin{cases} G_{\mathrm{ici}}=Z_{\mathrm{C}} Z_{\mathrm{L2}}, G_{\mathrm{u1i}}=Z_{\mathrm{L1}}+Z_{\mathrm{L2}}+Z_{\mathrm{L1}} Z_{\mathrm{C}} Z_{\mathrm{L2}} \\ G_{\mathrm{i1i}}=E+Z_{\mathrm{C}} Z_{\mathrm{L2}}, G_{\mathrm{u1u}}=E+Z_{\mathrm{C}} Z_{\mathrm{L1}},\ \ G_{\mathrm{u1u}}^{*}=E+Z_{\mathrm{C}}^{*} Z_{\mathrm{L1}}^{*} \end{cases} \tag{A3}$$

Time-delay transfer function, k_{pwm} is the equivalent gain of the inverter, and U_{base} is the PV inverter voltage base, and T_{de} is the time delay of SPWM:

$$\begin{cases} G_{\mathrm{de1}}=k_0 G_{\mathrm{de}} \\ G_{\mathrm{de}}=\left(1-0.75 T_{\mathrm{de}} s\right) /\left(1+0.75 T_{\mathrm{de}} s\right) \\ k_0=k_{\mathrm{pwm}} / U_{\mathrm{base}} \end{cases} \tag{A4}$$

PI transfer function of PV inverter:

$$\begin{cases} G_{\mathrm{PIu}}=k_{\mathrm{p\_pv}}+k_{\mathrm{i\_pv}} / s \\ G_{\mathrm{PIi}}=k_{\mathrm{p\_i}}+k_{\mathrm{i\_i}} / s \end{cases} \tag{A5}$$

k_{dc} is the DC-side base coefficient. Transfer function of u_2, i_2, i_{c} caused by PLL:

$$G_{\mathrm{P}}=G_{\mathrm{PIi}} G_{\mathrm{PIu}} k_{\mathrm{dc}} / s \tag{A6}$$

$$\begin{cases} G_{\mathrm{pll\_X}}^{\mathrm{s}}=\begin{bmatrix} 0 & X_{\mathrm{q}}^{\mathrm{s}} T_{\mathrm{pll}}^{\mathrm{s}} \\ 0 & -X_{\mathrm{d}}^{\mathrm{s}} T_{\mathrm{pll}}^{\mathrm{s}} \end{bmatrix},\ G_{\mathrm{pll\_X}}^{\mathrm{c}}=\begin{bmatrix} 0 & X_{\mathrm{q}}^{\mathrm{c}} T_{\mathrm{pll}}^{\mathrm{c}} \\ 0 & -X_{\mathrm{d}}^{\mathrm{c}} T_{\mathrm{pll}}^{\mathrm{c}} \end{bmatrix},\ X=u_2, i_2, i_{\mathrm{c}} \\ T_{\mathrm{pll}}^{\mathrm{s}}(s)=\dfrac{k_{\mathrm{p\_pll}} s+k_{i\_pll}}{s^2+U_{\mathrm{2d0}}^{\mathrm{s}}\left(k_{\mathrm{p\_pll}} s+k_{\mathrm{i\_pll}}\right)} \end{cases} \tag{A7}$$

$$G_{\mathrm{pll}}^{\mathrm{s}}=(G_{\mathrm{pll\_U2}}^{\mathrm{s}})^{-1} \tag{A8}$$

$$\begin{cases} G_{\mathrm{iref}}=\dfrac{k_{\mathrm{dc}}}{s} G_{\mathrm{PIu}}\begin{bmatrix} U_{\mathrm{1d}}^{\mathrm{s}} & U_{\mathrm{1q}}^{\mathrm{s}} \\ 0 & 0 \end{bmatrix} \\ G_{\mathrm{uref}}=\dfrac{k_{\mathrm{dc}}}{s} G_{\mathrm{PIu}}\begin{bmatrix} I_{\mathrm{1d}}^{\mathrm{s}} & I_{\mathrm{1q}}^{\mathrm{s}} \\ 0 & 0 \end{bmatrix} \end{cases} \tag{A9}$$

$$\begin{cases} G_{\mathrm{DC}}=G_{\mathrm{PIi}} G_{\mathrm{iref}} Z_{\mathrm{C}}+G_{\mathrm{PIi}} G_{\mathrm{uref}} G_{\mathrm{i1i}} \\ G_{\mathrm{AC\_s}}=G_{\mathrm{de1}}^{-1} G_{\mathrm{i1i}}+k_{\mathrm{C}} Z_{\mathrm{C}} \\ G_{\mathrm{AC\_pll}}=G_{\mathrm{de1}}^{-1} G_{\mathrm{pll\_U1}}^{\mathrm{s}}+G_{\mathrm{PIi}} G_{\mathrm{pll\_I2}}^{\mathrm{s}}+k_{\mathrm{C}} G_{\mathrm{pll\_Ic}}^{\mathrm{s}} \end{cases} \tag{A10}$$

$$G_{\mathrm{I}}=\begin{bmatrix} G_{\mathrm{PIi}}+k_{\mathrm{C}} G_{\mathrm{ici}}+G_{\mathrm{PIi}} G_{\mathrm{iref}} G_{\mathrm{i1i}} \\ +\left(G_{\mathrm{PIi}} G_{\mathrm{uref}}+G_{\mathrm{de1}}^{-1}\right) G_{\mathrm{u1i}} \end{bmatrix} \tag{A11}$$

Transfer function of adaptive control:

$$\begin{cases} F_0=\dfrac{s^2}{s^2+2 \xi \omega_0 s+\omega_0^2},\ \ F_1=\dfrac{1}{T_1 s+1} \\ F_{\mathrm{dc}}=\dfrac{s^2}{s^2+2 \xi \omega_{\mathrm{dc}} s+\omega_{\mathrm{dc}}^2}, G_{\mathrm{pll\_0}}=\dfrac{k_{\mathrm{p\_pll}} s+k_{\mathrm{i\_pll}}}{s^2+2 \xi \omega_0 s+\omega_0^2} \end{cases} \tag{A12}$$

$$\begin{cases} G_{\mathrm{A}}=\left(G_{\mathrm{u1u}}^{*} / k_0+k_{\mathrm{C}} Z_{\mathrm{C}}^{*}\right) G_{\mathrm{pll\_new}} \\ G_{\mathrm{B}}=\left(U_{\mathrm{1dq}}^{\mathrm{c}\ \mathrm{T}} / k_0+k_{\mathrm{C}} I_{\mathrm{cd}}^{\mathrm{c}\ \mathrm{T}}\right) G_{\mathrm{pll\_0}} \\ G_{\mathrm{C}}=I_{\mathrm{2dq}}^{\mathrm{c}\ \mathrm{T}} G_{\mathrm{pll\_0}} \\ G_{\mathrm{D}}=k_{\mathrm{dc}} F_{\mathrm{dc}} F_0 G_{\mathrm{P}} G_{\mathrm{pll\_new}} / s \end{cases} \tag{A13}$$

$$G_{\mathrm{U\_new}}=\left(1-F_{\mathrm{dc}} F_2 F_0\right) G_{\mathrm{DC}}+G_{\mathrm{AC\_new}} \tag{A14}$$

$$G_{\mathrm{pll\_new}}=\begin{bmatrix} F_0 & 0 \\ 0 & \dfrac{s^2+U_{\mathrm{2d}}\left(k_{\mathrm{p\_pll}} s+k_{\mathrm{i\_pll}}\right)}{s^2+2 \xi \omega_0 s+\omega_0^2} \end{bmatrix} \tag{A15}$$

$$\begin{cases} G_{\mathrm{AC\_new}}=G_{\mathrm{AC\_new1}}+G_{\mathrm{AC\_new2}}+G_{\mathrm{AC\_new3}} \\ G_{\mathrm{AC\_new1}}=\left(1-F_0 G_{\mathrm{de1}}\right)\left(G_{\mathrm{de1}}^{-1} G_{\mathrm{pll\_u1}}^{\mathrm{s}}\right) \\ G_{\mathrm{AC\_new2}}=\left(1-F_0\right)\left(F_1 G_{\mathrm{PIi}} G_{\mathrm{pll\_i2}}^{\mathrm{s}}+k_{\mathrm{C}} G_{\mathrm{pll\_ic}}^{\mathrm{s}}\right) \\ G_{\mathrm{AC\_new3}}=G_{\mathrm{de1}}^{-1} G_{\mathrm{u1u}}+k_{\mathrm{C}} G_{\mathrm{icu}}-F_0\left(G_{\mathrm{u1u}}^{*}+k_{\mathrm{C}} Z_{\mathrm{C}}^{*}\right) \end{cases} \tag{A16}$$

TABLE I. THE PARAMETERS OF PV STATION AND VSC

Parameters	Value
The rated capacity	600MVA
The control parameters of VSC	The proportional and integral parameters of PI for the outer loop, inner loop, and circulating current suppression are 1 and 200, 1 and 10, and 1 and 10, respectively;
The circuit parameters of VSC and AC lines	Arm inductor and resistor: 0.045H, 0.001Ω; Capacitance of each sub-module: 12e-3 F; Number of sub-modules: 200; L_{t1}=L_{t2}=0.05p.u. VSC Transformer inductor: 0.1p.u.; DC voltage: 400kV. The equivalent reactance and capacitance of the line per kilometer are 0.5 mH and 0.1 μF, respectively
The parameters of PV station	ω_0=30; ξ=1; ω_{dc}=10; T_1=0.01; L_1=0.2p.u.; L_2=0.1p.u.; C_{f}=0.0064p.u.; u_{pv}=2kV; C_{pv}=2F; $k_{\mathrm{p\_i}}$=;1 $k_{\mathrm{i\_i}}$=160; $k_{\mathrm{p\_pv}}$=1;$k_{\mathrm{i\_pv}}$=100

979-8-3315-8138-1